ELSEVIER

Comput. Methods Appl. Mech. Engrg. 174 (1999) 171–190

Computer methods in applied mechanics and engineering

A temperature-dependent beam for shape-memory alloys: constitutive modelling, finite-element implementation and numerical simulations

F. Auricchio[a,*] E. Sacco[b]

[a]*Dipartimento di Meccanica Strutturale, Università di Pavia, Via Ferrata 1, 27100 Pavia, Italy*
[b]*Dipartimento di Ingegneria Industriale, Università di Cassino, Via Di Biasio 43, 03043 Cassino, Italy*

Received 5 November 1997

Abstract

This paper presents a thermomechanical one-dimensional constitutive model based on the use of strain and temperature as control variables and able to reproduce the basic responses of shape-memory materials, such as superelasticity, the shape-memory behavior, different response in tension and compression, single-variant martensite reorientation process. The model time-integration is performed and a robust algorithm for the solution of the time-discrete model is addressed together with the algorithmically consistent tangent. The model is also implemented in a small-deformation beam finite-element, which is used to simulate the following applications exploiting the superelastic and/or the shape-memory effect: tensile, pure bending and three-point bending tests, orthodontic wires, two-way (linear and angular) mechanisms. The numerical investigations show that the proposed procedure is an effective computational tool for the simulation of a broad range of applications based on shape-memory materials.

1. Introduction

Shape-memory alloys (SMA) are materials able to undergo reversible changes of the crystallographic structure. As a consequence, depending on the temperature, they can recover large deformations during mechanical loading–unloading patterns (superelastic effect) or they can recover residual strains through thermal cycles (shape-memory effect) [1].

Due to the unusual macroscopic behavior, shape-memory alloys lend themselves to be used in innovative applications [1–3]. Examples of applications exploiting the superelastic effect range from orthodontic wires for the correction of teeth malpositions (orthodontic brackets) [4] to microstructures used in the treatment of blood-vessel occlusions (stents) [5]. Examples of applications exploiting the shape-memory effect range from devices driving the opening of spatial antennas or satellites [6] to moving mechanisms resembling micro-organisms [7].

As a consequence of the large interest toward the use of shape-memory materials, many constitutive models able to reproduce the main macroscopic effects have been proposed in literature. Some representative[1] works are by Abeyaratne and Knowles [8], Auricchio et al. [9–13], Barret and Sullivan [14,15], Boyd and Lagoudas [16], Brandon and Rogers [17], Brinson et al. [18,19], Falk and Kopka [20], Ivshin and Pence [21], Lexcellent et al.

* Corresponding author. E-mail: auricchio@ing.uniroma2.it

[1] But by no mean exhaustive of the literature richness on the subject.

0045-7825/99/$ – see front matter
PII: S0045-7825(98)00285-0

[22,23], Liang and Rogers [24,25], Muller and Xu [26], Patoor et al. [27–30], Raniecki and Lexcellent [31], Sun and Hwang [32,33], Tanaka et al. [34,35], Tobushi et al. [36] and Wilmanski [37].

However, there are only few examples of constitutive models able to reproduce the SMA material response and for which a proper numerical implementation is proposed. Examples are the work by Brinson and Lammering [38] and by Trochu and Qian [39].

On the other hand, there is a clear need of further developments in this direction, and in particular of robust numerical algorithms, to perform simulations of SMA devices under complex thermomechanical loading histories; as an example, you may consider the case of a stent undergoing the pulsing load due to the blood pressure as well as thermal excursions corresponding to the human body temperature.

Most of the proposed models assume stress as control variable. However, this choice may lead to quite complex situations during the attempt to solve shape-memory constitutive equations within the classical framework of finite-elements.

In fact, being finite-elements in general formulated as displacement driven, the solution of stress-controlled constitutive equations may require the development of complex algorithm in order to retain a clearly desired robustness [10,12].

According to this point of view, we assume strain and temperature as control variables and develop a time-continuous thermomechanical constitutive model, able to reproduce both the superelastic and the shape-memory effect. Time-integration of the model is then performed and a robust algorithm for the solution of the time-discrete model is proposed. Finally, the model is implemented in a small-deformation beam finite-element, which is used to simulate simple tests as well as applications exploiting the superelastic and shape-memory effect.

2. A one-dimensional superelastic and shape-memory constitutive equation

The shape-memory-alloy macroscopic behavior is the consequence of the material ability to change its crystallographic structure depending on the thermomechanical state.

These changes are, in general, interpreted as martensitic transformations between a crystallographically more-ordered phase, called *austenite*, and a crystallographically less-ordered phase, called *martensite*. The latter may be present in different but crystallographically equivalent forms (*variants*).

To describe the macroscopic consequence of these crystallographic changes, in the following we propose a one-dimensional constitutive model cast within the *generalized plasticity theory* [40]. As control variable, we choose the uniaxial strain, ε, and the temperature, T.

2.1. Phase transition and activation rules

We assume to describe the crystallographic state of the material through three scalar variables[2]:

- the multiple-variant martensite fraction, ξ_M
- the single-variant martensite fraction, ξ_S
- the austenite fraction, ξ_A

which should fulfill the following relation at any time:[3]

$$\xi_M + \xi_S + \xi_A = 1 \tag{1}$$

Consequently, only two fractions are independent, in the following chosen to be ξ_M and ξ_S. Accordingly, it is sufficient to describe only the evolution of these two independent parameters (for more details on this and related aspect you may refer to [9,12]) while the austenite fraction ξ_A may always be computed from Eq. (1).

Dealing with three material fractions, we consider the corresponding three production processes:

- production of multiple-variant-martensite,

[2] By convention, the capital letters M, S and A used as subscripts refer to specific fractions. In particular, $\xi_i = 0$ (with i = M, S, A) indicates absence of the corresponding phase in the material, while $\xi_i = 1$ indicates that the material is completely in that phase.

[3] For simplicity the dependency of the variables on a scalar parameter, such as time, is not explicitly stated.

- production of single-variant-martensite,
- production of austenite.

2.1.1. Production of multiple-variant martensite

The production of multiple-variant martensite can occur only as conversion (reduction) of austenite (A → M)[4]. We set

$$\dot{\xi}_{\mathrm{M}}^{\mathrm{AM}} = (\xi_{\mathrm{S}} + \xi_{\mathrm{M}} - 1)\mathscr{H}^{\mathrm{AM}} \frac{\dot{G}^{\mathrm{AM}}}{G^{\mathrm{AM}} - S_f^{\mathrm{AM}}} \tag{2}$$

where

$$\mathscr{H}^{\mathrm{AM}} = \begin{cases} 1 & \text{when } \begin{cases} \dot{G}^{\mathrm{AM}} < 0 \\ S_f^{\mathrm{AM}} \leqslant G^{\mathrm{AM}} \leqslant \mathrm{S}_s^{\mathrm{AM}} \end{cases} \\ 0 & \text{otherwise} \end{cases} \tag{3}$$

with

$$G^{\mathrm{AM}} = T\,, \qquad S_s^{\mathrm{AM}} = T_s^{\mathrm{AM}}\,, \qquad S_f^{\mathrm{AM}} = T_f^{\mathrm{AM}} \tag{4}$$

The quantities T_s^{AM} and T_f^{AM} are material parameters and represent the starting and final temperatures at which the transformation may occur at zero stress (Fig. 1).

2.1.2. Production of single-variant martensite

An increment of single-variant martensite can be obtained at the expenses of the austenite (A → S) and at the expenses of the multiple-variant martensite (M → S). Based on experimental evidences, we distinguish between the transformations occurring at temperatures less than T_s^{AM} and those occurring at temperatures greater than T_s^{AM} (Fig. 1).

In particular, we set

$$\dot{\xi}_{\mathrm{S},1}^{\mathrm{AS}} = (\xi_{\mathrm{S}} + \xi_{\mathrm{M}} - 1)\mathscr{H}_1^{\mathrm{AS}} \frac{\dot{G}_1^{\mathrm{AS}}}{G_1^{\mathrm{AS}} - S_{f,1}^{\mathrm{AS}}} \tag{5}$$

$$\dot{\xi}_{\mathrm{S},2}^{\mathrm{AS}} = (\xi_{\mathrm{S}} + \xi_{\mathrm{M}} - 1)\mathscr{H}_2^{\mathrm{AS}} \frac{\dot{G}_2^{\mathrm{AS}}}{G_2^{\mathrm{AS}} - S_{f,2}^{\mathrm{AS}}} \tag{6}$$

$$\dot{\xi}_{\mathrm{M},1}^{\mathrm{MS}} = \xi_{\mathrm{M}}\mathscr{H}_1^{\mathrm{AS}} \frac{\dot{G}_1^{\mathrm{AS}}}{G_1^{\mathrm{AS}} - S_{f,1}^{\mathrm{AS}}} \tag{7}$$

$$\dot{\xi}_{\mathrm{M},2}^{\mathrm{MS}} = \xi_{\mathrm{M}}\mathscr{H}_2^{\mathrm{AS}} \frac{\dot{G}_2^{\mathrm{AS}}}{G_2^{\mathrm{AS}} - S_{f,2}^{\mathrm{AS}}} \tag{8}$$

$$\dot{\xi}_{\mathrm{S},1}^{\mathrm{MS}} = -\xi_{\mathrm{M}}\mathscr{H}_1^{\mathrm{AS}} \frac{\dot{G}_1^{\mathrm{AS}}}{G_1^{\mathrm{AS}} - S_{f,1}^{\mathrm{AS}}} \tag{9}$$

$$\dot{\xi}_{\mathrm{S},2}^{\mathrm{MS}} = -\xi_{\mathrm{M}}\mathscr{H}_2^{\mathrm{AS}} \frac{\dot{G}_2^{\mathrm{AS}}}{G_2^{\mathrm{AS}} - S_{f,1}^{\mathrm{AS}}} \tag{10}$$

where:

[4] By convention, the superscripts refer to specific evolution processes; accordingly, the superscript AM refers to the conversion of austenite into multiple-variant martensite.

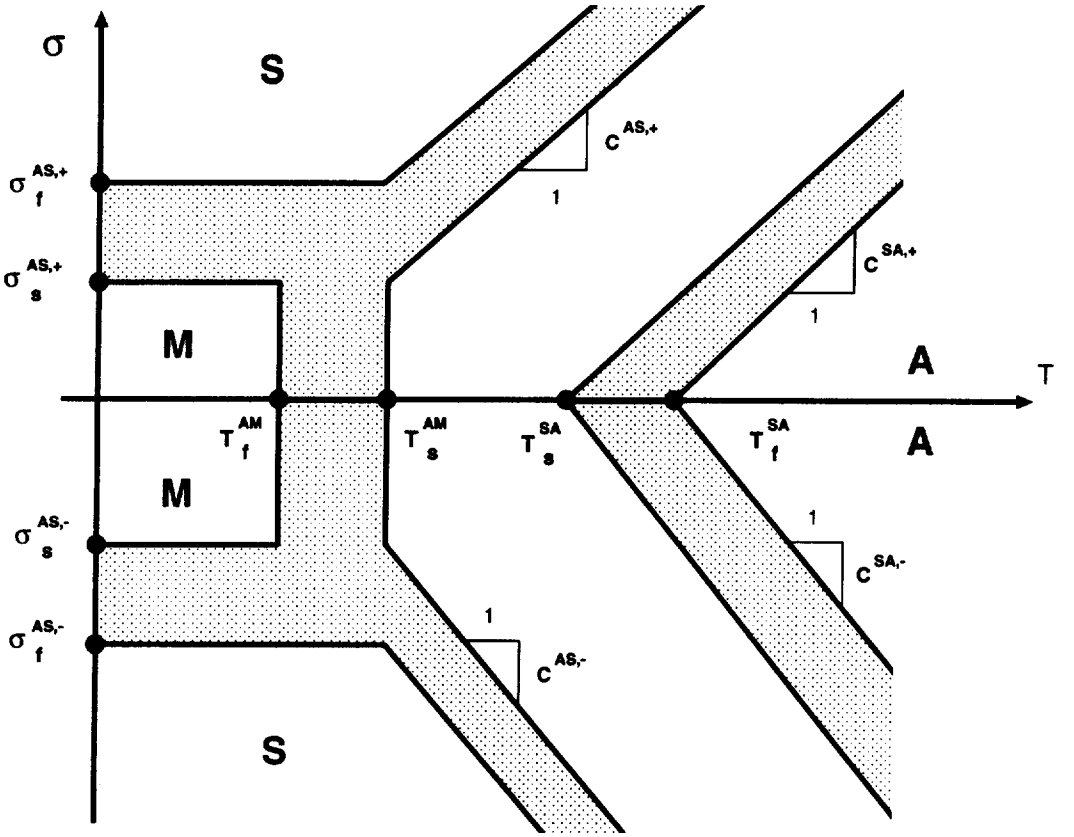

Fig. 1. Phase transformation zones in uniaxial tension and compression. Experimental investigations show that in a uniaxial stress–temperature diagram and in the usual range of applications the region in which phase transformations may occur (indicated in the figure with a dotted pattern) are delimited with good approximation by straight lines. We also indicate the regions in which only single fractions are stable (S: single-variant martensite, M: multiple-variant martensite, A: austenite).

$$\mathscr{H}_1^{AS} = \begin{cases} 1 & \text{when } \begin{cases} \dot{G}_1^{AS} > 0 \\ S_{s,1}^{AS} \leqslant G_1^{AS} \leqslant S_{f,1}^{AS} \end{cases} \text{ and } \quad G^{AM} \leqslant G_s^{AM} \\ 0 & \text{otherwise} \end{cases} \tag{11}$$

$$\mathscr{H}_2^{AS} = \begin{cases} 1 & \text{when } \begin{cases} \dot{G}_2^{AS} > 0 \\ S_{s,2}^{AS} \leqslant G_2^{AS} \leqslant S_{f,2}^{AS} \end{cases} \text{ and } \quad G^{AM} \leqslant G_s^{AM} \\ 0 & \text{otherwise} \end{cases} \tag{12}$$

with

$$\begin{aligned} G_1^{AS} &= |\varepsilon|, & S_{s,1}^{AS} &= \frac{R_{s,1}^{AS}}{E} + \varepsilon_L \xi_S, & S_{f,1}^{AS} &= \frac{R_{f,1}^{AS}}{E_S} + \varepsilon_L \\ G_2^{AS} &= |\varepsilon| - D^{AS} T, & S_{s,2}^{AS} &= \frac{R_{s,2}^{AS}}{E} + \varepsilon_L \xi_S, & S_{f,2}^{AS} &= \frac{R_{f,2}^{AS}}{E_S} + \varepsilon_L \end{aligned} \tag{13}$$

being ε_L the recoverable strain[5] $D^{AS} = C^{AS}/E$ with C^{AS} the Clausius–Clapeyron constant for the phase transformation $A \rightarrow S$ (Fig. 1) and E the Young's modulus. Since in general the initial and final values of the

[5] The recoverable strain or maximum residual strain, ε_L, regarded as a material constant, is a measure of the maximum deformation obtainable only by multiple-variant martensite detwinning, hence, a measure of the maximum deformation obtainable aligning all the single-variant martensites in one direction [41,18].

phase transformations are expressed in terms of stress, the following relations are introduced:

$$\begin{aligned} R_{s,1}^{\mathrm{AS}} &= \sigma_s^{\mathrm{AS}}, & R_{f,1}^{\mathrm{AS}} &= \sigma_f^{\mathrm{AS}} \\ R_{s,1}^{\mathrm{AS}} &= \sigma_s^{\mathrm{AS}} - C^{\mathrm{AS}} T_s^{\mathrm{AM}}, & R_{f,1}^{\mathrm{AS}} &= \sigma_f^{\mathrm{AS}} - C^{\mathrm{AS}} T_s^{\mathrm{AM}} \end{aligned} \tag{14}$$

The quantities σ_s^{AS}, σ_f^{AS}, C^{AS} and ε_L are all material parameters (Fig. 1)[6].

2.1.3. Production of austenite

An increment of austenite can be obtained at the expenses of the multiple-variant martensite (M → A) and at the expenses of the single-variant martensite (S → A). We distinguish between the two conversion processes, also if the zones in which they may occur are assumed to be identical.

In particular, we set

$$\dot{\xi}_{\mathrm{S}}^{\mathrm{SA}} = \xi_{\mathrm{S}} \mathscr{H}^{\mathrm{SA}} \frac{\dot{G}^{\mathrm{SA}}}{G^{\mathrm{SA}} - S_f^{\mathrm{SA}}} \tag{15}$$

$$\dot{\xi}_{\mathrm{M}}^{\mathrm{MA}} = \xi_{\mathrm{M}} \mathscr{H}^{\mathrm{SA}} \frac{\dot{G}^{\mathrm{SA}}}{G^{\mathrm{SA}} - S_f^{\mathrm{SA}}} \tag{16}$$

where

$$\mathscr{H}^{\mathrm{SA}} = \begin{cases} 1 & \text{when } \begin{cases} \dot{G}^{\mathrm{SA}} < 0 \\ S_f^{\mathrm{SA}} \leqslant G^{\mathrm{SA}} \leqslant S_s^{\mathrm{SA}} \end{cases} \\ 0 & \text{otherwise} \end{cases} \tag{17}$$

with

$$G^{\mathrm{SA}} = |\varepsilon| - D^{\mathrm{SA}} T, \qquad S_s^{\mathrm{SA}} = \frac{R_s^{\mathrm{SA}}}{E} + \varepsilon_L \xi_{\mathrm{S}}, \qquad S_f^{\mathrm{SA}} = \frac{R_f^{\mathrm{SA}}}{E_{\mathrm{A}}} \tag{18}$$

being $D^{\mathrm{SA}} = C^{\mathrm{SA}}/E$ with C^{SA} the Clapeyron constant for the phase transformation S → A (Fig. 1). The following relations also hold:

$$R_s^{\mathrm{SA}} = -C^{\mathrm{SA}} T_s^{\mathrm{SA}}, \qquad R_f^{\mathrm{SA}} = -C^{\mathrm{SA}} T_f^{\mathrm{SA}} \tag{19}$$

The quantities T_s^{SA}, T_f^{SA} and C^{SA} are material parameters.

REMARK 2.1. Because of the general framework in which the model is developed [40], there is no limitation on the relative position of the phase-transition zones; hence they may intersect or they may be disjoint, since neither case would be problematic.

REMARK 2.2. Taking into account the previous remark and [9,42], we set

$$\begin{aligned} \dot{\xi}_{\mathrm{S}} &= \dot{\xi}_{\mathrm{S},1}^{\mathrm{AS}} + \dot{\xi}_{\mathrm{S},2}^{\mathrm{AS}} + \dot{\xi}_{\mathrm{S},1}^{\mathrm{MS}} + \dot{\xi}_{\mathrm{S},2}^{\mathrm{MS}} + \dot{\xi}_{\mathrm{S}}^{\mathrm{SA}} \\ \dot{\xi}_{\mathrm{M}} &= \dot{\xi}_{\mathrm{M}}^{\mathrm{AM}} + \dot{\xi}_{\mathrm{M},1}^{\mathrm{MS}} + \dot{\xi}_{\mathrm{M},2}^{\mathrm{MS}} + \dot{\xi}_{\mathrm{M}}^{\mathrm{MA}} \end{aligned} \tag{20}$$

REMARK 2.3. The evolutionary equations so far introduced are strain and temperature controlled; in fact, the loading functions G^{AM}, G_1^{AS}, G_2^{AS}, G^{SA} depend only on strain and temperature. This choice differs from what is usually proposed in the literature, where the evolutionary equation loading functions depend on stress and temperature.

[6] For the distinction of material parameters between tension and compression, indicated in Fig. 1 with superscripts + or −, and the relative discussion, see Remark 2.4.

2.2. Strain decomposition and martensite reorientation

We assume an additive decomposition of the strain between a quota due to the elastic response of the material, a quota due to the phase transformations and a quota due to the thermal expansion. Recalling that only the single-variant martensite can give a contribution to the strain [41], we set

$$\varepsilon = \varepsilon^e + \xi_S \beta + \alpha(T - T_0) \tag{21}$$

where α is the thermal expansion coefficient, T_0 is a reference temperature and β is an internal variable describing the orientation of the martensite. Being in a one-dimensional setting, β represents the change of martensite orientation corresponding to a change from tension to compression or vice versa.

Different models can be introduced to describe such a reorientation process. In the following we consider a very simple mechanism governed by the following evolutionary equation:

$$\dot{\beta} = \mathcal{H}^{SS} \gamma [\varepsilon_L \operatorname{sgn}(\sigma) - \beta](\sigma - \sigma^{SS}) \tag{22}$$

with

$$\mathcal{H}^{SS} = \begin{cases} 1 & \text{when } |\sigma| > \sigma^{SS} \\ 0 & \text{otherwise} \end{cases} \tag{23}$$

where γ is a material parameter measuring the velocity of the reorientation process.

2.3. Elastic relation

We choose a linear elastic stress-strain relation; taking into account Eq. (21), we set

$$\sigma = E[\varepsilon - \xi_S \beta - \alpha(T - T_0)] \tag{24}$$

Due to the experimentally observed difference between the austenite and the martensite elastic properties, a dependence of the elastic modulus E on the martensite fraction is introduced. In particular, recalling Auricchio and Sacco [10], the following functional form is adopted:

$$E(\xi) = \frac{E_A E_S}{E_S + \xi(E_A - E_S)} \tag{25}$$

where E_A and E_S are, respectively, the austenite and the martensite elastic moduli.

REMARK 2.4. Experimental evidences show that shape-memory materials behave quite differently in tension and compression. Recalling that we are dealing with a one-dimensional constitutive model, to obtain this effect, it is sufficient to distinguish between a set of material parameters valid in tension (indicated in the following with a superscript $+$) and a set of material parameters valid in compression (indicated in the following with a superscript $-$).

Accordingly, we have:

$$C^{AS,+}, \quad C^{SA,+}, \quad \sigma_s^{AS,+}, \quad \sigma_f^{AS,+}, \quad \varepsilon_L^+, \quad \sigma^{SS,+}$$
$$C^{AS,-}, \quad C^{SA,-}, \quad \sigma_s^{AS,-}, \quad \sigma_f^{AS,-}, \quad \varepsilon_L^-, \quad \sigma^{SS,+}$$

The material parameters E_A, E_S, T_s^{AM} T_f^{AM}, T_s^{SA} and T_f^{SA} are assumed to be equal in tension and compression.

However, in the following the superscripts $+$ or $-$ are omitted for brevity whenever confusion is not induced. The whole set of material parameters is indicated in Fig. 1.

3. Time-discrete model and solution algorithm

From a computational standpoint we treat the non-linear material behavior as a *time-discrete strain-driven* problem. Accordingly, we first introduce a time-discrete counterpart of the constitutive model addressed in the

previous section and then discuss the possibility to compute the stress from the strain history by means of a *return-map* algorithm.

3.1. Time-discrete model

Let $[0, T] \subset \mathscr{R}$ be the time interval of interest and consider two time values within it, say t_n and $t_{n+1} > t_n$, such that t_{n+1} is the first time value of interest after t_n. To minimize the appearance of subscripts, the subscript n indicates a quantity that is evaluated at time t_n, while no subscript indicates a quantity that is evaluated at time t_{n+1}.

The time-discrete model is obtained integrating over the time interval $[t_n, t_{n+1}]$ the rate equations described in Section 2. In particular, using a backward Euler scheme, the time-discrete counterpart of Eqs. (2), (5)–(10), (15)–(16) in residual form are:

$$\begin{cases} R_{\mathrm{S}}^1 = \lambda_{\mathrm{S}}^1 (G_1^{\mathrm{AS}} - S_{f,1}^{\mathrm{AS}}) + (1 - \xi_{\mathrm{M}} - \xi_{\mathrm{S}})(G_1^{\mathrm{AS}} - G_{1,n}^{\mathrm{AS}})\mathscr{H}_1^{\mathrm{AS}} = 0 \\ R_{\mathrm{S}}^2 = \lambda_{\mathrm{S}}^1 (G_1^{\mathrm{AS}} - S_{f,1}^{\mathrm{AS}}) + \xi_{\mathrm{M}} (G_1^{\mathrm{AS}} - G_{1,n}^{\mathrm{AS}})\mathscr{H}_1^{\mathrm{AS}} = 0 \\ R_{\mathrm{S}}^3 = \lambda_{\mathrm{S}}^3 (G_2^{\mathrm{AS}} - S_{f,2}^{\mathrm{AS}}) + (1 - \xi_{\mathrm{M}} - \xi_{\mathrm{S}})(G_2^{\mathrm{AS}} - G_{2,n}^{\mathrm{AS}})\mathscr{H}_2^{\mathrm{AS}} = 0 \\ R_{\mathrm{S}}^4 = \lambda_{\mathrm{S}}^4 (G_2^{\mathrm{AS}} - S_{f,2}^{\mathrm{AS}}) + \xi_{\mathrm{M}} (G_2^{\mathrm{AS}} - G_{2,n}^{\mathrm{AS}})\mathscr{H}_2^{\mathrm{AS}} = 0 \\ R_{\mathrm{S}}^5 = \lambda_{\mathrm{S}}^5 (G^{\mathrm{AS}} - S_f^{\mathrm{AS}}) - \xi_{\mathrm{S}} (G^{\mathrm{SA}} - G_n^{\mathrm{SA}})\mathscr{H}^{\mathrm{SA}} = 0 \\ R_{\mathrm{M}}^1 = \lambda_{\mathrm{M}}^1 (G^{\mathrm{AM}} - S_f^{\mathrm{AM}}) + (1 - \xi_{\mathrm{M}} - \xi_{\mathrm{S}})(G^{\mathrm{AM}} - G_n^{\mathrm{AM}})\mathscr{H}^{\mathrm{AM}} = 0 \\ R_{\mathrm{M}}^2 = \lambda_{\mathrm{M}}^2 (G_1^{\mathrm{AS}} - S_{f,1}^{\mathrm{AS}}) - \xi_{\mathrm{M}} (G_1^{\mathrm{AS}} - G_{1,n}^{\mathrm{AS}})\mathscr{H}_1^{\mathrm{AS}} = 0 \\ R_{\mathrm{M}}^3 = \lambda_{\mathrm{M}}^3 (G_2^{\mathrm{AS}} - S_{f,2}^{\mathrm{AS}}) - \xi_{\mathrm{M}} (G_1^{\mathrm{AS}} - G_{2,n}^{\mathrm{AS}})\mathscr{H}_2^{\mathrm{AS}} = 0 \\ R_{\mathrm{M}}^4 = \lambda_{\mathrm{M}}^4 (G^{\mathrm{SA}} - S_f^{\mathrm{SA}}) - \xi_{\mathrm{M}} (G^{\mathrm{SA}} - G_n^{\mathrm{SA}})\mathscr{H}^{\mathrm{SA}} = 0 \end{cases} \tag{26}$$

where

$$\begin{aligned} &\lambda_{\mathrm{S}}^1 = \int_{t_n}^{t_{n+1}} \dot{\xi}_{\mathrm{S},1}^{\mathrm{AS}}\, \mathrm{d}t\,, \qquad \lambda_{\mathrm{S}}^2 = \int_{t_n}^{t_{n+1}} \dot{\xi}_{\mathrm{S},1}^{\mathrm{MS}}\, \mathrm{d}t\,, \qquad \lambda_{\mathrm{S}}^3 = \int_{t_n}^{t_{n+1}} \dot{\xi}_{\mathrm{S},2}^{\mathrm{AS}}\, \mathrm{d}t \\ &\lambda_{\mathrm{S}}^4 = \int_{t_n}^{t_{n+1}} \dot{\xi}_{\mathrm{S},2}^{\mathrm{AS}}\, \mathrm{d}t\,, \qquad \lambda_{\mathrm{S}}^5 = \int_{t_n}^{t_{n+1}} \dot{\xi}_{\mathrm{S}}^{\mathrm{SA}}\, \mathrm{d}t\,, \qquad \lambda_{\mathrm{M}}^1 = \int_{t_n}^{t_{n+1}} \dot{\xi}_{\mathrm{M}}^{\mathrm{AM}}\, \mathrm{d}t \\ &\lambda_{\mathrm{M}}^2 = \int_{t_n}^{t_{n+1}} \dot{\xi}_{\mathrm{M},1}^{\mathrm{MS}}\, \mathrm{d}t\,, \qquad \lambda_{\mathrm{M}}^3 = \int_{t_n}^{t_{n+1}} \dot{\xi}_{\mathrm{M},2}^{\mathrm{MS}}\, \mathrm{d}t\,, \qquad \lambda_{\mathrm{M}}^4 = \int_{t_n}^{t_{n+1}} \dot{\xi}_{\mathrm{M}}^{\mathrm{MA}}\, \mathrm{d}t \end{aligned} \tag{27}$$

Eq. (26) can also be written in a matrix compact form:

$$\begin{cases} \boldsymbol{R}_{\mathrm{S}} = \boldsymbol{R}_{\mathrm{S}}(\boldsymbol{\lambda}_{\mathrm{S}}, \boldsymbol{\lambda}_{\mathrm{M}}) = 0 \\ \boldsymbol{R}_{\mathrm{M}} = \boldsymbol{R}_{\mathrm{M}}(\boldsymbol{\lambda}_{\mathrm{S}}, \boldsymbol{\lambda}_{\mathrm{M}}) = 0 \end{cases} \tag{28}$$

where

$$\begin{aligned} \boldsymbol{R}_{\mathrm{S}} &= \{R_{\mathrm{S}}^1, R_{\mathrm{S}}^2, R_{\mathrm{S}}^3, R_{\mathrm{S}}^4, R_{\mathrm{S}}^5\}^{\mathrm{T}} \\ \boldsymbol{R}_{\mathrm{M}} &= \{R_{\mathrm{M}}^1, R_{\mathrm{M}}^2, R_{\mathrm{M}}^3, R_{\mathrm{M}}^4\}^{\mathrm{T}} \\ \boldsymbol{\lambda}_{\mathrm{S}} &= \{\lambda_{\mathrm{S}}^1, \lambda_{\mathrm{S}}^2, \lambda_{\mathrm{S}}^3, \lambda_{\mathrm{S}}^4, \lambda_{\mathrm{S}}^5\}^{\mathrm{T}} \\ \boldsymbol{\lambda}_{\mathrm{M}} &= \{\lambda_{\mathrm{M}}^1, \lambda_{\mathrm{M}}^2, \lambda_{\mathrm{M}}^3, \lambda_{\mathrm{M}}^4\}^{\mathrm{T}} \end{aligned} \tag{29}$$

Integration of Eq. (20) return:

$$\begin{aligned} \xi_{\mathrm{S}} &= \xi_{\mathrm{S},n} + \lambda_{\mathrm{S}}^1 + \lambda_{\mathrm{S}}^2 + \lambda_{\mathrm{S}}^3 + \lambda_{\mathrm{S}}^4 + \lambda_{\mathrm{S}}^5 \\ \xi_{\mathrm{M}} &= \xi_{\mathrm{M},n} + \lambda_{\mathrm{M}}^1 + \lambda_{\mathrm{M}}^2 + \lambda_{\mathrm{M}}^3 + \lambda_{\mathrm{M}}^4 \end{aligned} \tag{30}$$

which can be also written as

$$\xi_S = \xi_{S,n} + \sum_{i=1,5} \lambda_S^i = \xi_{S,n} + \mathbf{1}_5 \cdot \boldsymbol{\lambda}_S \tag{31}$$

$$\xi_M = \xi_{M,n} + \sum_{i=1,4} \lambda_M^i = \xi_{M,n} + \mathbf{1}_4 \cdot \boldsymbol{\lambda}_M \tag{32}$$

where:

$$\begin{aligned} \mathbf{1}_5 &= \{1, 1, 1, 1, 1\} \\ \mathbf{1}_4 &= \{1, 1, 1, 1\} \end{aligned} \tag{33}$$

Integration of Eq. (22) governing the reorientation process gives

$$\beta = \beta_n + H^{SS}\, \Delta t\, \gamma[\varepsilon_L\, \mathrm{sgn}(\sigma) - \beta](\sigma - \sigma^{SS}) \tag{34}$$

Finally, the elastic stress–strain relation is directly evaluated at time t_{n+1}:

$$\sigma = E[\varepsilon - \xi_S \beta - \alpha(T - T_0)] \tag{35}$$

3.2. Return-map algorithm

The time-discrete nonlinear problem so far addressed is now solved using a return-map algorithm. The solution at time t_n is assumed to be known, together with the strain ε at time t_{n+1}.

The return-map is, in general, a two-step procedure of the type elastic-predictor inelastic-corrector, used for the integration of elastoplastic constitutive equations [43]. However, due to the specific model now investigated, a classical two-step return-map is not adequate as solution scheme.

In fact, two are the aspects which make our problem completely different from elastoplasticity and, hence, that need to be carefully addressed in order to develop a robust solution algorithm:

- the evolutionary processes here considered are phase transformations; accordingly, for each of them there exist conditions at which the evolution is completed (exhausted). This results in a non-connected elastic domain, as clearly discussed in [40].
- multiple phase transformations may be active at the same time

Details of the solution algorithm for the time-discrete model proposed are reported in Table 1.

If the conditions for the phase transformations are satisfied (Step 2), the new martensite fraction is computed solving Eqs. (26) through a Newton iterative scheme:

$$\begin{aligned} \begin{Bmatrix} \boldsymbol{\lambda}_S^{k+1} \\ \boldsymbol{\lambda}_M^{k+1} \end{Bmatrix} &= \begin{Bmatrix} \boldsymbol{\lambda}_S^{k} \\ \boldsymbol{\lambda}_M^{k} \end{Bmatrix} - \begin{bmatrix} L_{SS} & L_{SM} \\ L_{MS} & L_{MM} \end{bmatrix}^{-1} \begin{Bmatrix} \boldsymbol{R}_S(\boldsymbol{\lambda}_S^k, \boldsymbol{\lambda}_M^k) \\ \boldsymbol{R}_M(\boldsymbol{\lambda}_S^k, \boldsymbol{\lambda}_M^k) \end{Bmatrix} \\ &= \begin{Bmatrix} \boldsymbol{\lambda}_S^{k} \\ \boldsymbol{\lambda}_M^{k} \end{Bmatrix} - \begin{bmatrix} A_{SS} & A_{SM} \\ A_{MS} & A_{MM} \end{bmatrix} \begin{Bmatrix} \boldsymbol{R}_S(\boldsymbol{\lambda}_S^k, \boldsymbol{\lambda}_M^k) \\ \boldsymbol{R}_M(\boldsymbol{\lambda}_S^k, \boldsymbol{\lambda}_M^k) \end{Bmatrix} \end{aligned} \tag{36}$$

where the superscripts ^{k} and $^{k+1}$ indicate the iteration indices and

Table 1
Return-map solution algorithm for the time-discrete model

1. Test on complete transformation
   (a) Check consistency of strain and temperature with a complete-transformation state
   (b) If check is satisfied, then skip step 2
2. Martensite update
   (a) Check conditions for the activation of any phase transformation
   (b) If check satisfied, then compute new solution for martensite fraction
3. Reorientation update
   (a) Check conditions for activation of reorientation process
   (b) If check satisfied, then compute new orientation

$$\boldsymbol{L}_{ij} = \frac{\partial \boldsymbol{R}_i}{\partial \boldsymbol{\lambda}_j} \quad \text{with} \quad i = \text{S, M and } j = \text{S, M} \tag{37}$$

If the conditions for the reorientation process are satisfied (Step 3), the new martensite orientation is also computed through a Newton iterative scheme.

3.3. Time-discrete tangent

For future developments, we now compute the algorithmically tangent moduli, that is we linearize the stress constitutive equation in terms of the strain. Starting from Eq. (35), we get

$$\mathrm{d}\sigma = \{[E^*(\varepsilon - \xi_S \beta) - E\beta]A + E - E\xi_S B\}\,\mathrm{d}\varepsilon \tag{38}$$

where the quantities:

$$E^* = \frac{\partial E}{\partial \xi_S}, \qquad A = \frac{\partial \xi_S}{\partial \varepsilon}, \qquad B = \frac{\partial \beta}{\partial \varepsilon} \tag{39}$$

can be computed as follows:

- recalling Eq. (25), we get

$$E^* = -E^2 \frac{E_A - E_S}{E_A E_S} \tag{40}$$

- We start noting that:

$$\frac{\partial \xi_S}{\partial \varepsilon} = \frac{\partial \lambda_S}{\partial \varepsilon} = \sum_{i=1,5} \frac{\lambda_S^i}{\partial \varepsilon} = \mathbf{1}_5 \frac{\partial \boldsymbol{\lambda}_S}{\partial \varepsilon} \tag{41}$$

Now, linearizing Eq. (26) as function of $\boldsymbol{\lambda}_S$, $\boldsymbol{\lambda}_M$ and ε:

$$\mathrm{d}\boldsymbol{R}_S = \frac{\partial \boldsymbol{R}_S}{\partial \boldsymbol{\lambda}_S}\mathrm{d}\boldsymbol{\lambda}_S + \frac{\partial \boldsymbol{R}_S}{\partial \boldsymbol{\lambda}_M}\mathrm{d}\boldsymbol{\lambda}_M + \frac{\partial \boldsymbol{R}_S}{\partial \varepsilon}\mathrm{d}\varepsilon = \mathbf{0} \tag{42}$$

$$\mathrm{d}\boldsymbol{R}_M = \frac{\partial \boldsymbol{R}_M}{\partial \boldsymbol{\lambda}_S}\mathrm{d}\boldsymbol{\lambda}_S + \frac{\partial \boldsymbol{R}_M}{\partial \boldsymbol{\lambda}_M}\mathrm{d}\boldsymbol{\lambda}_M + \frac{\partial \boldsymbol{R}_M}{\partial \varepsilon}\mathrm{d}\varepsilon = \mathbf{0} \tag{43}$$

and recalling Eq. (36), we get

$$\begin{Bmatrix} \mathrm{d}\boldsymbol{\lambda}_S \\ \mathrm{d}\boldsymbol{\lambda}_M \end{Bmatrix} = -\begin{bmatrix} \boldsymbol{A}_{SS} & \boldsymbol{A}_{SM} \\ \boldsymbol{A}_{MS} & \boldsymbol{A}_{MM} \end{bmatrix} \begin{Bmatrix} \dfrac{\partial \boldsymbol{R}_S}{\partial \varepsilon}\mathrm{d}\varepsilon \\ \dfrac{\partial \boldsymbol{R}_M}{\partial \varepsilon}\mathrm{d}\varepsilon \end{Bmatrix} \tag{44}$$

Accordingly

$$\mathrm{d}\boldsymbol{\lambda}_S = -\left(\boldsymbol{A}_{SS}\frac{\partial \boldsymbol{R}_S}{\partial \varepsilon} + \boldsymbol{A}_{SM}\frac{\partial \boldsymbol{R}_M}{\partial \varepsilon}\right)\mathrm{d}\varepsilon \tag{45}$$

The latter expression plugged into Eq. (41) returns the final expression for A.

- Finally, $B = \partial\beta/\partial\varepsilon$ can be computed from the linearization of the time-discrete evolutionary equations governing the reorientation process (Eq. (34)), resulting in

$$B = \frac{Z\{E + A[E^*(\varepsilon - \xi_S\beta) - E\beta]\}}{1 + E\xi_S Z} \tag{46}$$

where

$$Z = H^{SS}\,\Delta t\,\gamma[\varepsilon_L\,\mathrm{sgn}(\sigma) - \beta] \tag{47}$$

4. A finite-element beam

We now develop a finite-element formulation for a beam made of a shape-memory material, whose constitutive behavior is described through the model presented in the previous section.

A classical small-deformation Euler–Bernoulli beam theory is herein adopted [44]. The beam occupies a volume V, has cross-section A and length L. We indicate with (x, y, z) a Cartesian coordinate system having the x-axis coincident with the centerline axis of the undeformed beam. The x-y plane is also a plane of symmetry for the problem, such that the beam can undergo only elongation and deflection within this plane.

4.1. Kinematics and temperature field

Following the Euler–Bernoulli beam theory, the cross-sections are assumed to remain plane and orthogonal to the centerline of the deformed beam. The beam kinematics and deformation are defined as

$$\begin{aligned} u &= u_0(x) - y v_0'(x) && \text{axial displacement} \\ v &= v_0(x) && \text{transversal displacement} \\ \varepsilon &= \varepsilon_0 - y\chi && \text{strain} \end{aligned} \tag{48}$$

where a superscript $'$ indicates a derivative with respect to x, while $\varepsilon_0 = u_0'$ and $\chi_0 = v_0''$ are the elongation and the curvature, respectively.

Moreover, in the present work we assume to neglect the production of thermal energy associated to the material fraction evolutions. According to this position, we retain the temperature as a given field (control variable); in particular, recalling the symmetry condition on the x-y plane, the thermal field is set to be linear in the cross section with y and constant along the beam axis:

$$T = \frac{T_d - T_u}{h}\, y + \frac{T_d + T_u}{2} \tag{49}$$

where T_d and T_u are, respectively, the temperature at the beam bottom and top, while h is the beam height.

4.2. Equilibrium equations

The beam equilibrium equations are derived introducing the kinematical assumptions into the principle of virtual displacement $L_{ve} = L_{vi}$, where L_{ve} and L_{vi} are the external and the internal virtual works, respectively.

In particular, using Eq. (48) the internal virtual work reduces to

$$\begin{aligned} L_{vi} &= \int_V \sigma\, \delta\varepsilon \, \mathrm{d}V = \int_L \int_A [\sigma \delta(\varepsilon_0 - y\chi)] \, \mathrm{d}A \, \mathrm{d}x \\ &= \int_L [N \, \mathrm{d}\varepsilon_0 + M \, \delta\chi] \, \mathrm{d}x \end{aligned} \tag{50}$$

where the axial force N and the bending moment M are defined as

$$N = \int_A \sigma \, \mathrm{d}A\,, \qquad M = -\int_A y\sigma \, \mathrm{d}A \tag{51}$$

Written in residual form, Eq. (51) can be considered as the cross-section equilibrium equations.

4.3. Finite-element interpolation

The finite-element formulation is performed introducing an approximation on the displacement fields (u, v). The axial displacement u is taken linear along the beam axis, while the transversal displacement v is interpolated by the classical Hermite shape functions as required by the Euler–Bernoulli beam theory.

Substitution of the interpolation functions in the principle of virtual work returns the finite-element beam equilibrium equations. These nonlinear equations are first written in residual form and then are solved through a Newton algorithm [45]. For the development of the Newton algorithm the following steps are required:

Table 2
Iteration procedure for the solution of the equilibrium equations

```
do until [(residual on beam equil. eqns) ≤ tol1]
  initialize beam quantities
  loop on Gauss points along beam length
    compute ε0, χ at specific Gauss point
    do until [(residual on cross-section equil. eqns) ≤ tol2]
      initialize cross-section quantities
      loop on elements in the cross section
        loop on Gauss points per element
          compute strain ε
          compute martensite fraction ξ
          compute stress σ
          add contribution to N and M
          compute algorithmic tangent moduli
          add contribution to global tangent
        end loop
      end loop
    end do
  end loop
  compute new ε0, χ nodal solution
end do
```

(1) time integration of the local constitutive equations
(2) solution algorithm for the time-discrete equations
(3) determination of the algorithmically tangent moduli (i.e. $\partial\sigma/\partial\varepsilon$)
(4) evaluation of the line and area integrals

Steps 1, 2 and 3 have been discussed in detail in Sections 3.1, 3.2 and 3.3, respectively. The integration along the beam axis is performed numerically by Gauss formulas; the integration over the cross-section is performed discretizing the cross-section in strip elements orthogonal to the y-axis and applying Gauss formulas within each strip.

The adopted Newton scheme consists of two nested loops: the outer one relative to the satisfaction of the beam global equilibrium equations, the inner one relative to the satisfaction of the cross-section beam equations.[7] The algorithmic implementation of the iterative procedure is briefly reported in Table 2.

5. Numerical simulations

We now consider several examples to assess the performances of the proposed procedure in studying structures made of shape-memory materials.

Initially, the attention is concentrated on the response of single cross-sections, i.e. the axial force and the bending moment are taken constant along the beam axis. We then investigate more general examples, e.g. three-point bending tests as well as two-way (linear and angular) mechanisms.

All the structures considered are supposed to be made of a commercial Ni–Ti wire produced by GAC International Inc. and having a rectangular cross-section of dimension $h = 0.64$ mm and $b = 0.46$ mm. This specific alloy has been experimentally investigated by Airoldi and coworkers in tensile and three-point bending conditions [46].

Using a series of tensile tests reported in Fig. 2 of Airoldi et al. [46], we set the following tensile properties[8]:

[7] For a more detailed discussion of the linearization and solution algorithm for the cross-section equilibrium equations, you may refer to Auricchio and Sacco [11].

[8] In literature the initial temperature for the A→S phase transformation at zero stress and the final temperature for the S→A phase transformation at zero stress are indicated as M_s and A_f, respectively. However, we use the symbols T_s^{AM} and T_f^{SA}, respectively, for consistency with the other constitutive-model material constants.

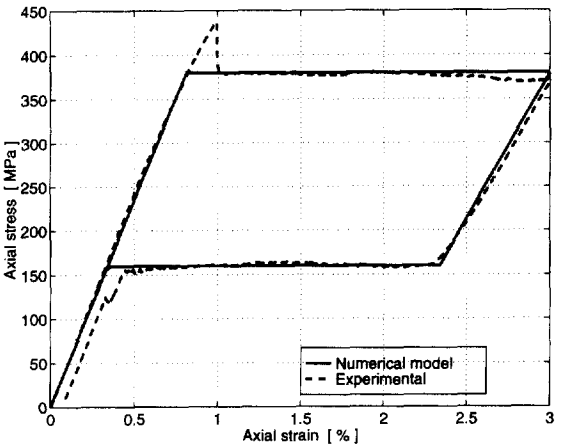

Fig. 2. Uniaxial test: superelastic behavior. Axial stress versus axial strain. Comparison between experimental data (dashed line) and numerical simulation (continuous line).

$$
\begin{aligned}
&E_A = 47\,000\ \text{MPa}, && E_S = 17\,000\ \text{MPa}\\
&\sigma_s^{AS,+} = \sigma_f^{AS,+} = 140\ \text{MPa}, && \sigma^{SS,+} = 30\ \text{MPa}\\
&C^{AS,+} = 6\ \text{MPa/°C}, && C^{SA,+} = 8\ \text{MPa/°C}\\
&T_s^{AM} = 10\text{°C}, && T_f^{AM} = 5\text{°C}\\
&T_s^{SA} = T_f^{SA} = 30\text{°C}, && \varepsilon_L^{+} = 0.08^\circ
\end{aligned}
\tag{52}
$$

It is important to point out that the assessment of the constitutive-model material constants from the experimental data reported in [46] is a difficult and by no means exhaustive process; in fact, the tests were originally not designed for this goal. Hence, even for the tensile case, the constants reported in (52) have some degree of discretionality; as an example, the choice of the total recoverable strain ε_L^+ is arbitrary and clearly it affects the global structural response investigated in the following.

Moreover, the uniaxial data available in [46] are all relative to tensile states. As a consequence, the determination of the constitutive-model constants for the compressive range are obtained in part extrapolating results relative to a Ni–Ti–Cu alloy [47].[9] Accordingly, we set

$$
\begin{aligned}
&\sigma_s^{AS,-} = \sigma_f^{AS,-} = 196\ \text{MPa}, && \sigma^{SS,-} = 40\ \text{MPa}\\
&C^{AS,-} = 8.4\ \text{MPa/°C}, && C^{SA,-} = 11.2\ \text{MPa/°C}\\
&\varepsilon_L^{-} = 0.06\%, && \gamma = 1\ \text{MPa/sec}
\end{aligned}
\tag{53}
$$

In the following, all the tests are simulated starting from an initial temperature T_0, corresponding to an unstrained, unstressed and fully austenitic state.

Finally, the numerical integration along the beam length is performed using 4 Gauss points per element. The cross-section integrals are computed dividing each section in 20 strips and using 4 Gauss points in each strip.

5.1. Uniaxial response

We start simulating a uniaxial test to show the ability of the constitutive model to properly reproduce the superelastic and the shape-memory effect. T_0 is assumed equal to 50°C.

[9] For some remarks on the difference between the material response in tension and compression, you may also refer to Auricchio et al. [12].

5.1.1. Superelastic effect

Keeping the temperature constant ($T = 50°C$), the material is subjected to a simple tensile loading-unloading history, inducing only a partial conversion of austenite into martensite.

Fig. 2 shows the uniaxial stress–strain response together with the corresponding experimental data. The result obtained from a uniaxial test inducing a full transformation both in tension and in compression is reported in Fig. 3.

It is interesting to observe: (1) the ability to completely recover the deformation during the unloading being at a temperature above T_f^{SA}, i.e. the ability to reproduce the superelastic effect in a uniaxial state of stress; (2) the different transformation values as well as the different size of the hysteresis loop between tension and compression; (3) the different elastic moduli between austenite and martensite.

5.1.2. Shape-memory effect

Keeping fixed the axial strain ($\varepsilon_0 = 0\%$), we initially cool the specimen from 50°C to 0°C. Then, keeping fixed the temperature ($T = 0°C$), we perform a complete loading–unloading pattern in term of axial strain. Finally, keeping again fixed the axial strain ($\varepsilon_0 = 0\%$), we heat the specimen back to $T = 50°C$.

Fig. 4 shows the material response in terms of stress, strain and temperature [thick line] as well as in terms of stress–strain (projection on a plane with constant temperature) and stress–temperature (projection on a plane with constant strain) [thin lines].

It is interesting to observe: (1) the stress arises during the initial cooling at zero strain; (2) the presence of a residual stress at the end of the loading–unloading pattern being at temperature below T_f^{AM}; (3) the ability to completely recover the initial state (zero stress, zero strain) during the final heating process reaching a temperature above T_f^{SA}, i.e. the ability to reproduce the shape-memory effect in a uniaxial state of stress.

5.2. Pure bending response

The goal of this second series of tests is to investigate the response of a SMA beam under pure bending ($N = 0$). Again, the analysis are performed both in the superelastic and in the shape-memory range. T_0 is assigned equal to 50°C.

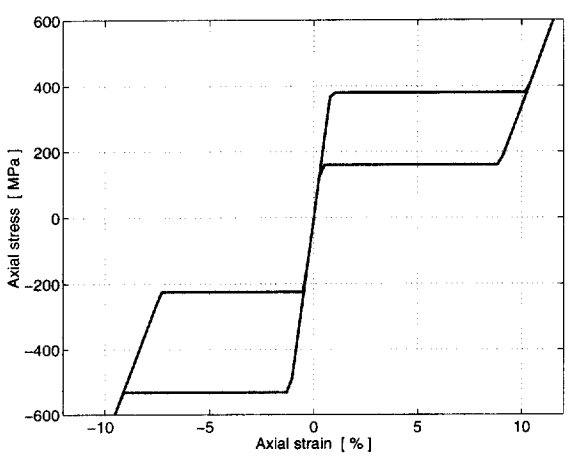

Fig. 3. Uniaxial test: superelastic behavior in tension and compression. Axial stress versus axial strain. It is noted: (1) the ability to completely recover the deformation; (2) the different tensile and compressive response; (3) the different elastic moduli between austenite and martensite.

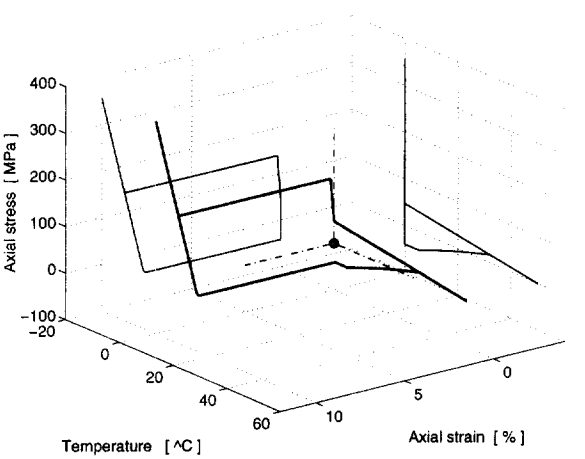

Fig. 4. Uniaxial test: shape-memory behavior. Stress–strain–temperature [thick line]. The response in terms of stress–strain (projection on a plane with constant temperature) and in terms of stress–temperature (projection on a plane with constant strain) is also reported [thin lines]. The position of a reference coordinate system is also indicated [dot-dash line]. At the end of the mechanical loading–unloading the specimen shows a residual stress, which is completely recovered by heating.

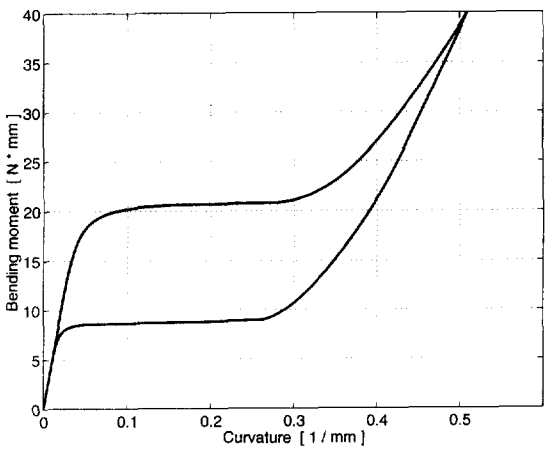

Fig. 5. Pure bending test: superelastic behavior. Moment versus curvature. The beam shows the ability to completely recover the curvature during the unloading.

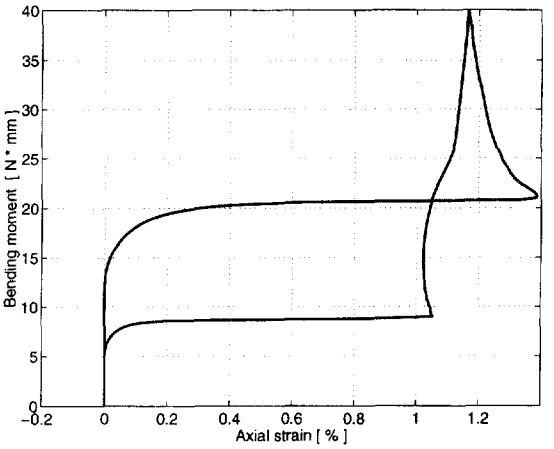

Fig. 6. Pure bending test: superelastic behavior. Moment versus axial strain. It is interesting to observe: (1) the non-monotonic response even during the loading part; (2) the ability to completely recover also the axial deformation during the unloading.

5.2.1. *Superelastic effect*

Keeping the temperature constant ($T = 50°C$), the beam is subjected to a loading–unloading history in terms of applied bending moment. Figs. 5 and 6 show the bending moment M versus the curvature χ and the axial strain ε_0, respectively.

It is interesting to observe: (1) the ability to completely recover the deformation during the unloading being at a temperature above T_f^{SA}, that is, the ability to reproduce the superelastic effect also in a bending state; (2) the non-monotonic response of the axial strain with respect to the moment, even during the loading path.

This second effect can be well interpreted looking at the stress distribution over the cross-section for different loading levels. During the loading the stress distribution in the cross-section evolves as discussed in the following.

(1) At the beginning no phase transformation occurs in the cross-section. Thus, the material response is linearly elastic and the neutral axis remains at zero.

(2) Since the value of the $A \rightarrow S$ stress transformation is higher in compression than in tension, the phase transformation starts first on the part of the cross-section in traction. Accordingly, to obtain a zero axial resultant, the neutral axis starts to move upward and an axial deformation shows up.

(3) As soon as the phase transformation is completed on the part of the cross-section in traction, a material restiffening is encountered. Hence, a progressive downward movement of the neutral axis occurs, together with an axial deformation reduction. In general, during the loading it is even possible to observe a stress reduction in part of the cross-section, leading to the activation of the reverse $S \rightarrow A$ phase transformation.

For a more detailed discussion about the stress profile evolution during superelastic pure bending test, you may refer to Auricchio and Sacco [11].

5.2.2. *Shape-memory effect*

Keeping fixed the curvature ($\chi = 0\,\text{mm}^{-1}$), we initially cool the beam from 50°C to 0°C. Then, keeping fixed the temperature ($T = 0°C$), we perform a complete loading–unloading pattern in term of curvature. Finally, keeping again fixed the curvature ($\chi = 0\,\text{mm}^{-1}$), we heat the specimen back to 50°C.

Figs. 7 and 8 show the moment–curvature–temperature and the elongation–curvature–temperature responses, respectively [thick line]. The moment-curvature (projection on a plane with constant temperature) and the moment-temperature (projection on a plane with constant curvature) responses are also reported [thin lines].

It is interesting to observe: (1) the axial strain arise during the initial cooling; (2) the presence of a residual moment at the end of the loading–unloading pattern; (3) the ability to completely recover the initial state (zero

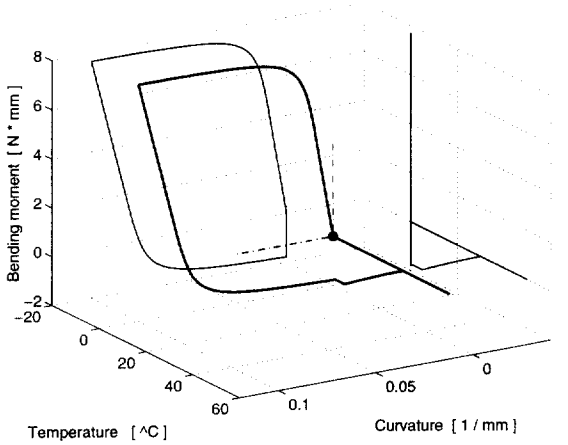

Fig. 7. Pure bending test: shape-memory behavior. Moment–curvature–temperature [thick line]. The response in terms of moment–curvature (projection on a plane with constant temperature) and in terms of moment–temperature (projection on a plane with constant curvature) is also reported [thin lines]. The position of a reference coordinate system is also indicated [dot-dash line]. At the end of the mechanical loading–unloading the specimen shows a residual moment, which is completely recovered by heating.

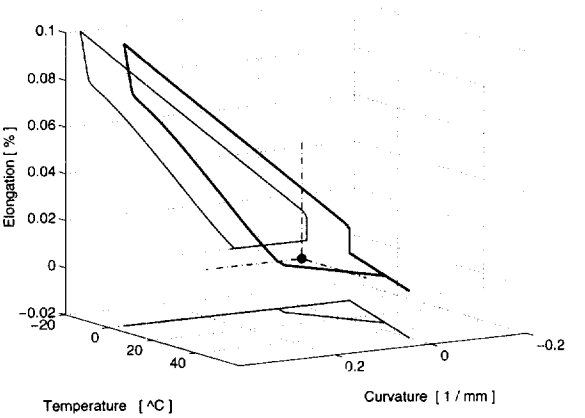

Fig. 8. Pure bending test: shape-memory behavior. Elongation–curvature–temperature [thick line]. The response in terms of elongation–curvature (projection on a plane with constant temperature) and in terms of curvature–temperature (projection on a plane with constant elongation) is also reported [thin lines]. The position of a reference coordinate system is also indicated [dot-dash line]. At the end of the mechanical loading–unloading the specimen shows a residual elongation, which is completely recovered by heating.

moment, zero curvature, zero axial strain) during the final heating process reaching a temperature above T_f^{SA}, that is, the ability to reproduce the shape-memory effect also in a bending state.

5.3. Three-point bending test

Following Reference [Airoldi et al. [46]] we study the behavior of a simply supported beam subjected to a pointwise central force (three-point bending test). The beam has length $L = 14$ mm and, due to symmetry conditions, only half of the beam is discretized using a mesh of 10 elements.

Again, we investigate the structural response in the superelastic and in the shape memory range.

5.3.1. Superelastic test

A complete loading–unloading test is simulated at two different temperature, $T = T_0 = 55$°C and $T = T_0 = 37$°C. The comparison between the numerical solution and the experimental results is presented in terms of the applied force versus the midspan inflection in Figs. 9 and 10, respectively.

It is interesting to observe the better match obtained at the higher temperature; the difference between the numerical and experimental results during the initial portion of the unloading can be attributed to effects not taken into account in the present analysis, such as rate-dependency of the shape-memory response or slip mechanisms of the beam over the supports.[10]

5.3.2. Shape-memory test

Keeping fixed the midspan inflection ($u = 0$ mm), we initially cool the beam from 50°C to 0°C. Then, keeping fixed the temperature ($T = 0$°C), we perform a complete loading–unloading pattern in term of midspan inflection. Finally, keeping again fixed the midspan inflection ($u = 0$ mm), we heat the beam back to 50°C.

Fig. 11 shows the applied force versus midspan displacement and temperature [thick line]. The load–

[10] In fact, in the finite-element model the beam is assumed to be simply supported at the end cross-sections, while in the experimental setting the test is performed using two supports at fixed distance and the beam seat and slide on them at the same time.

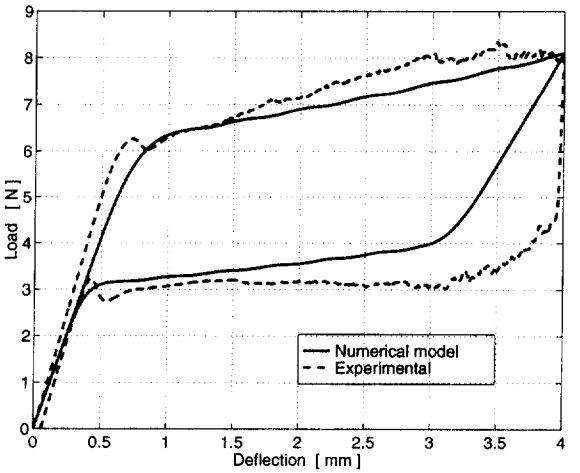

Fig. 9. Three-point bending test at $T = 55°C$: superelastic behavior. Applied force versus midspan deflection. Comparison between experimental data and numerical simulation. The beam shows the ability to completely recover the deformation during the unloading.

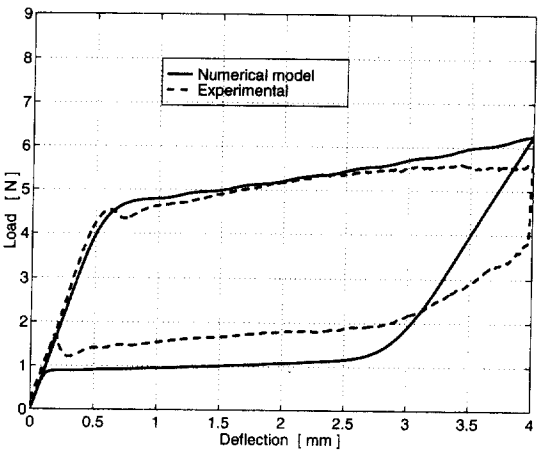

Fig. 10. Three-point bending test at $T = 37°C$: superelastic behavior. Applied force versus midspan deflection. Comparison between experimental data and numerical simulation. The beam shows the ability to completely recover the deformation during the unloading.

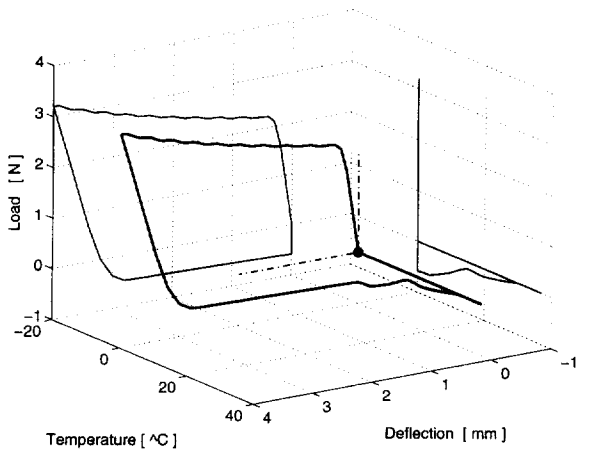

Fig. 11. Three-point bending test: the shape-memory effect. Applied force versus midspan deflection and temperature [thick line]. The load–deflection (projection on a plane with constant temperature) and the load–temperature (projection on a plane with constant curvature) responses are also reported [thin lines]. The position of a reference coordinate system is also indicated [dot-dash line]. The beam shows the ability to completely recover the deformation during the final thermal treatment.

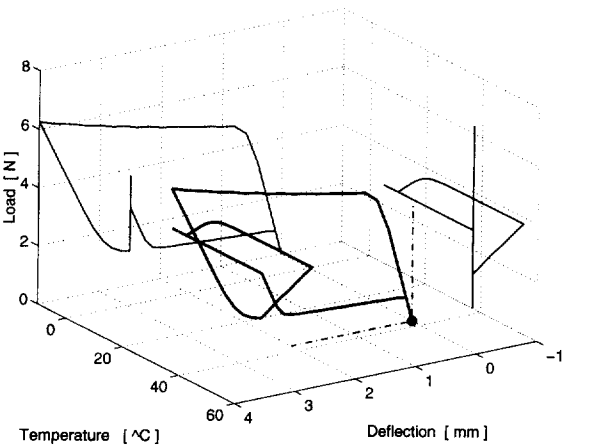

Fig. 12. Orthodontic wire. Applied force versus midspan deflection and temperature [thick line]. The load–deflection (projection on a plane with constant temperature) and the load–temperature (projection on a plane with constant curvature) responses are also reported [thin lines]. The position of a reference coordinate system is also indicated [dot-dash line]. The temperature cycle performed at fixed deflection ($d = 2.5$ mm) induces a change in the recovery force.

deflection (projection on a plane with constant temperature) and the load–temperature (projection on a plane with constant curvature) responses are also reported [thin lines].

It is interesting to observe: (2) the presence of a residual force at the end of the loading–unloading pattern; (3) the ability to completely recover the initial state (zero moment, zero curvature) during the final heating process reaching a temperature above T_f^{SA}, that is, the ability to reproduce the shape-memory effect also in a three-point bending state.

5.4. Orthodontic wires

The use of SMA superelastic properties for the correction of teeth malocclusions in orthodontics is a very successful application, since it allows to obtain an optimal teeth movement as well as to control and drastically shorten the therapy [4].

However, the temperature in the oral cavity is frequently modified as a consequence of meal and food intakes. This leads to very complex loading patterns and, in general, to changes in the recovery forces acting on the teeth with possible consequent painful sensations.

Following the experimental investigations performed by Airoldi and coworkers [46], a three-point bending test is simulated to study the force variation of an orthodontic archwire consequent to drink intake. The beam described in the previous section is again considered and T_0 is set equal to 37°C.

The thermomechanical loading history consists of three steps:

(1) Keeping fixed the temperature $T = 37°C$, the specimen is loaded up to a deflection of 4 mm and partially unloaded to a deflection of 2.5 mm, representing the initial phase of therapy

(2) Keeping fixed the deflection, the specimen undergoes the following thermal pattern:

$$37°C \rightarrow 55°C \rightarrow 5°C \rightarrow 37°C$$

representing the intake of a hot meal followed by the intake of a cold drink.

(3) Finally, the unloading process is completed

Fig. 12 shows the force variation in terms of deflection and temperature. The load–deflection (projection on a plane with constant temperature) and the load–temperature (projection on a plane with constant deflection) responses are also reported [thin lines].

It is interesting to observe how the numerical solution is able to reproduce the experimentally observed changes in the recovery force as a consequence of the intake of hot/cold quantities.

5.5. A two-way linear mechanism

The shape–memory effect investigated so far is a one-way effect, that is, the recovery of the original (undeformed) shape can be obtained thermally only once and only after the material has been mechanically deformed.

However, there is a simple way to obtain a two-way shape-memory effect, that is, the ability to switch back and forth between two configurations simply through thermal cycles. This effect can be obtained coupling a SMA wire (or spring) with a bias system, obtaining for example a mechanism of the type indicated in Fig. 13. In particular, we set $L = 10$ mm and $T_0 = 100°C$.

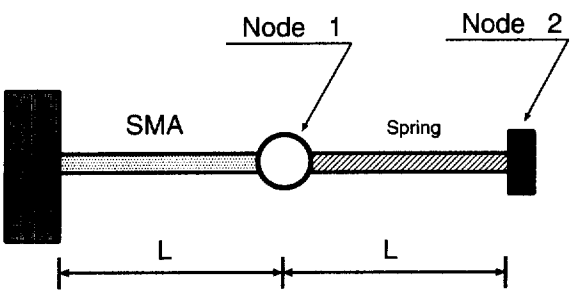

Fig. 13. Two-way linear mechanism. Device geometry.

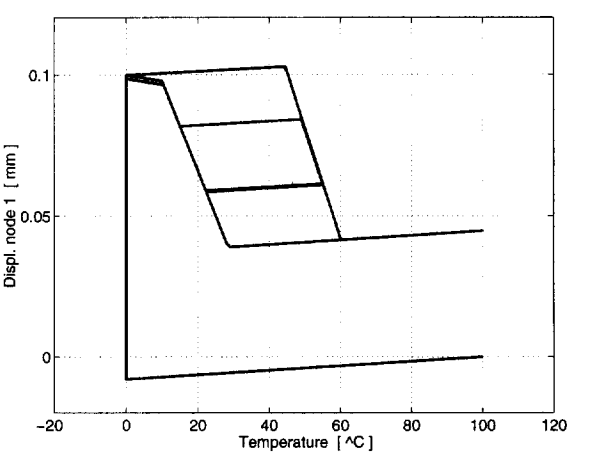

Fig. 14. Two-way linear mechanism. Displacement of central node versus temperature.

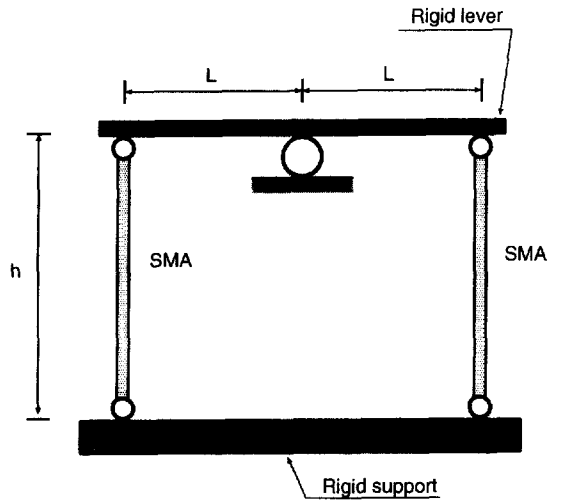

Fig. 15. Two-way angular mechanism. Device geometry.

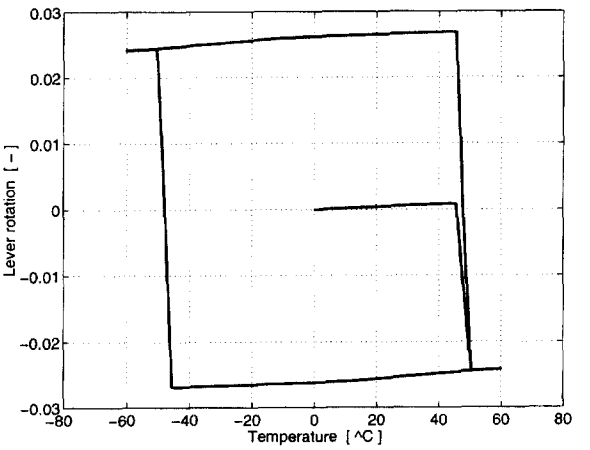

Fig. 16. Two-way angular mechanism. Lever rotation versus temperature differential.

The applied loading history is the following.

(1) Keeping fixed node 2, we cool the mechanism from 100°C to 0°C
(2) Keeping fixed the temperature at 0°C, we displace node 2 by 0.15 mm
(3) Keeping fixed node 2, we now perform three thermal cycles, the first one inducing a full transformation in the SMA wire, the other two inducing only partial transformations.

The displacement of node 1 versus the temperature is plotted in Fig. 14. It is interesting to observe how it is possible to control the position of node 1 through the imposed thermal cycles.[11]

5.6. A two-way angular mechanism

A different two-way mechanism is the one proposed in Fig. 15. We now have a rigid lever and two shape-memory wires hinged to a rigid support ($L = 5$ mm, $h = 10$ mm). We indicate the temperature of the wire on the right with T_R and the temperature of the wire on the left with T_L, being ΔT the temperature differential (i.e. $\Delta T = T_L - T_R$).

The applied loading history is described in the following.

(1) Keeping fixed the rigid support, we cool the mechanism from 60°C to 0°C
(2) Keeping fixed the temperature at 0°C, we displace the rigid support by 1 mm
(3) Keeping fixed the rigid support, we now perform the following thermal cycles:

Time	1	2	3	4	5	6	7	8	9
T_L	0	60	0	0	0	60	0	0	0
T_R	0	0	0	60	0	0	0	60	0
ΔT	0	60	0	−60	0	60	0	−60	0

The lever rotation in terms of temperature differential is reported in Fig. 16. It is interesting to observe the possibility of controlling the lever rotation through the temperature differential.

[11] For a more accurate discussion on the use of shape-memory materials as actuator you may refer to Duerig et al. [48] and Tautzenberger [49].

6. Conclusions

The present work proposes a computation tool for the design of SMA-based devices. The tool is based on three main ingredients:

(1) a 1D thermomechanical constitutive model able to reproduce the basic macroscopic features of shape-memory materials, such as superelasticity, the shape-memory behavior, different response in tension and compression, single-variant-martensite reorientation process.
(2) the integration in time of the 1D model and the development of a robust solution algorithm for the time-discrete model
(3) the combination of this solution algorithm with a small-deformation beam finite-element

The second aspect is of crucial importance of complex thermomechanical loading histories should be taken into account, as it is the case for SMA structures.

To assess the viability of the proposed approach we simulate the following applications exploiting the superelastic and/or the shape-memory effect: tensile, pure bending and three-point bending tests, orthodontic wires, two-way (linear and angular) mechanisms.

The numerical investigations show that the proposed procedure is an effective computational tool for the simulation of a broad range of applications based on shape-memory materials.

References

[1] T.W. Duerig, M.N. Melton, D. Stökel and C.M. Wayman, eds., Engineering Aspects of Shape Memory Alloys (Butterworth-Heinemann, 1990).
[2] A.R. Pelton, D. Hodgson and T. Duerig, eds., Proc. First Int. Conf. on Shape Memory and Superelastic Technologies, Asilomar, CA, 1995.
[3] A.R. Pelton, D. Hodgson and T. Duerig, eds., Proc. Second Int. Conf. on Shape Memory and Superelastic Technologies, Asilomar, CA, 1997.
[4] R.C.L. Sachdeva and S. Miyazaki, Superelastic Ni–Ti alloys in orthodontics, in: T.W. Duerig, M.N. Melton, D. Stökel and C.M. Wayman, eds., Engineering Aspects of Shape Memory Alloys (1990) 452–469.
[5] A. Melzer and D. Stökel, Performance improvement of surgical instrumentation through the use of Ni–Ti materials, in: A.R. Pelton, D. Hodgson and T. Duerig, eds., Proc. First Int. Conf. on Shape Memory and Superelastic Technologies (1994) 401–409.
[6] L. Schetky, Shape memory alloy applications in space systems, in: T.W. Duerig, K.N. Melton, D. Stökel and C.M. Wayman, eds., Engineering Aspects of Shape Memory Alloys (1990) 170–177.
[7] G.B. Olson, Introduction: martensite in perspective, in: G.B. Olson and W.S. Owen, eds., Martensite: A Tribute to Morris Cohen (1992) 1–10.
[8] R. Abeyaratne and J.K. Knowles, A continuum model of thermoelastic solid capable of undergoing phase transitions, J. Mech. Phys. Solids 41 (1993) 541–571.
[9] F. Auricchio and J. Lubliner, A uniaxial model for shape-memory alloys, Int. J. Solids Struct. 34 (1997) 3601–3618.
[10] F. Auricchio and E. Sacco, A 1D model for superelastic shape-memory alloys with different elastic properties between austenite and martensite, Int. J. Nonlinear Mech. 32 (1997) 1101–1114.
[11] F. Auricchio and E. Sacco, A superelastic shape-memory-alloy beam, J. Intell. Mater. Struct. 8 (1997) 489–501.
[12] F. Auricchio, R.L. Taylor and J. Lubliner, Shape-memory alloys: macromodelling and numerical simulations of the superelastic behavior, Comput. Methods Appl. Mech. Engrg. 146 (1997) 281–312.
[13] F. Auricchio and R.L. Taylor, Shape-memory alloys: modelling and numerical simulations of the finite-strain superelastic behavior, Comput. Methods Appl. Mech. Engrg. 143 (1997) 175–194.
[14] D.J. Barret, A one-dimensional constitutive model for shape-memory alloys, J. Intelligent Mater. Syst. Struct. 6 (1995) 329–337.
[15] D.J. Barret and B.J. Sullivan, A three-dimensional phase transformation model for shape-memory alloys, J. Intelligent Mater. Syst. Struct. 6 (1995) 831–839.
[16] J.G. Boyd and D.C. Lagoudas, A thermodynamical constitutive model for shape-memory materials. Part I. The monolithic shape-memory alloy, Int. J. Plasticity 12 (1996) 805–842.
[17] D. Brandon and R.C. Rogers, Constitutive laws for pseudo-elastic materials, J. Intelligent Mater. Syst. Struct. 3 (1992) 255–267.
[18] L.C. Brinson, One-dimensional constitutive behavior of shape memory alloys: Thermomechanical derivation with non-constant material functions and redefined martensite internal variables, J. Intelligent Mater. Syst. Struct. 4 (1993) 229–242.
[19] L.C. Brinson, A. Bekker and S. Hwang, Deformation of shape memory alloys due to thermo-induced transformations, J. Intelligent Mater. Syst. Struct. 7 (1996) 97–107.
[20] F. Falk and P. Konopka, Three-dimensional Landau theory describing the martensitic phase transformation of shape-memory alloys, J. Phys.: Condensed Matter 2 (1990) 61–77.
[21] Y. Ivshin and J. Pence, A constitutive model for hysteretic phase transition behavior, Int. J. Engrg. Sci. (1994) 681–704.

[22] C. Lexcellent, B.C. Goo, Q.P. Sun and J. Bernardini, Characterization, thermomechanical behaviour and micromechanical-based constitutive model of shape-memory Cu–Zn–Al single crystals, Acta Mater. 44 (1996) 3773–3780.
[23] B.C. Goo and C. Lexcellent, Micromechanics-based modeling of two-way memory effect of a single crystalline shape-memory alloy, Acta Mater. 45 (1997) 727–737.
[24] C. Liang and C.A. Rogers, One-dimensional thermomechanical constitutive relations for shape memory materials, J. Intelligent Mater. Syst. Struct. 1 (1990) 207–234.
[25] C. Liang and C.A. Rogers, A multi-dimensional constitutive model for shape memory alloys, J. Engrg. Math. 26 (1992) 429–443.
[26] I. Muller and H. Xu, On the pseudo-elastic hysteresis, Acta Metall. et Materialia 39 (1991) 263–271.
[27] E. Patoor, A. Eberhardt and M. Berveiller, Thermomechanical behaviour of shape memory alloys, Arch. Mech. 40 (1988) 755–794.
[28] E. Patoor, N. Siredey, A. Eberhardt and M. Berveiller, Micromechanical approach of the fatique behavior in a superelastic single crystal, J. de Physique IV C8-5 (1995) 227–232.
[29] D. Entemeyer, E. Patoor, A. Eberhardt and M. Berveiller, Micromechanical modelling of the superthermoelastic behavior of materials undergoing thermoelastic phase transition, J. de Physique IV C8-5 (1995) 233–238.
[30] E. Patoor, A. Eberhardt and M. Berveiller, Micromechanical modelling of superelasticity in shape memory alloys, J. de Physique IV C8-5 (1995) 277–292.
[31] B. Raniecki and C. Lexcellent, R_L-models of pseudoelasticity and their specification for some shape memory solids, Europ. J. Mech. A/Solids 13 (1994) 21–50.
[32] Qing Ping Sun and Keh Chih Hwang, Micromechanics modelling for the constitutive behavior of polycrystalline shape memory alloys. I. Derivation of general relations, J. Mech. Phys. Solids 41 (1993) 1–17.
[33] Qing Ping Sun and Keh Chih Hwang, Micromechanics modelling for the constitutive behavior of polycrystalline shape memory alloys. II. Study of the individual phenomena, J. Mech. Phys. Solids 41 (1993) 19–33.
[34] K. Tanaka, A thermomechanical sketch of shape memory effect: one-dimensional tensile behavior, Res Mechanica 18 (1986) 251–263.
[35] K. Tanaka, T. Hayashi, Y. Itoh and H. Tobushi, Analysis of thermomechanical behavior of shape memory alloys, Mech. Mater. 13 (1992) 207–215.
[36] H. Tobushi, H. Iwanaga, K. Tanaka, T. Hori and T. Sawada, Deformation behavior of TiNi shape memory alloy subjected to variable stress and temperature, Continuum Mech. Thermodyn. 3 (1991) 79–93.
[37] K. Wilmanski, Symmetric model of stress-strain hysteresis loops in shape memory alloys, Int. J. Engrg. Sci. 31 (1993) 1121–1138.
[38] L.C. Brinson and R. Lammering, Finite-element analysis of the behavior of shape-memory alloys and their applications, Int. J. Solids Struct. 30 (1993) 3261–3280.
[39] F. Trochu and Y.Y. Qian, Nonlinear finite element simulation of superelastic shape-memory alloy parts, Computers & Structures, 62 (1991) 799–810.
[40] J. Lubliner and F. Auricchio, Generalized plasticity and shape memory alloys, Int. J. Solids Struct. 33 (1996) 991–1003.
[41] C.M. Wayman, Introduction to the Crystallography of Martensitic Transformations (MacMillan, 1964).
[42] F. Auricchio, SHAPE-MEMORY ALLOYS: Applications, micromechanics, macromodelling and numerical simulations, Ph.D. Dissertation, University of California at Berkeley, Department of Civil Engineering, 1995.
[43] J.C. Simo, Topics on the numerical analysis and simulation of plasticity, in: P.G. Ciarlet and J.L. Lions, eds., Handbook of Numerical Analysis, Vol. III (Elsevier, 1994).
[44] E.P. Popov, Engineering Mechanics of Solids (Prentice Hall, Englewood Cliffs, NJ, 1990).
[45] D.G. Luenberger, Introduction to Linear and Nonlinear Programming (Addison-Wesley Publishing Company, 1984).
[46] G. Airoldi, G. Riva and M. Vanelli, Superelasticity and shape-memory effect in Ni–Ti orthodontic wires, in: Proc. Int. Conf. on Martensitic Transformations, ICOMAT, 1995.
[47] P.H. Adler, W. Yu, A.R. Pelton, R. Zadno, T.W. Duerig and R. Barresi, On the tensile and torsional properties of pseudoelastic Ni–Ti, Scripta Metall. et Materialia 24 (1990) 943–947.
[48] T.W. Duerig, D. Stökel and A. Keeley, Actuator and work production devices, in: T.W. Duerig, M.N. Melton, D. Stökel and C.M. Wayman, eds., Engineering Aspects of Shape Memory Alloys (1990) 181–194.
[49] P. Tautzenberger, Thermal actuators: a comparison of shape memory alloys with thermostatic bimetals and wax actuators, in: T.W. Duerig, K.N. Melton, D. Stökel and C.M. Wayman, eds., Engineering Aspects of Shape Memory Alloys (1990) 207–218.